JACS
JOURNAL OF THE AMERICAN CHEMICAL SOCIETY
pubs.acs.org/JACS
Article

Control over Charge Separation by Imine Structural Isomerization in Covalent Organic Frameworks with Implications on CO_2 Photoreduction

Daniel H. Streater, Eric R. Kennehan, Denan Wang, Christian Fiankor, Liangji Chen, Chongqing Yang, Bo Li, Daohua Liu, Faysal Ibrahim, Ive Hermans, Kevin L. Kohlstedt, Long Luo, Jian Zhang, and Jier Huang*

Cite This: https://doi.org/10.1021/jacs.3c10627

ABSTRACT: Two-dimensional covalent organic frameworks (COFs) are an emerging class of photocatalytic materials for solar energy conversion. In this work, we report a pair of structurally isomeric COFs with reversed imine bond directions, which leads to drastic differences in their physical properties, photophysical behaviors, and photocatalytic CO_2 reduction performance after incorporating a $Re(bpy)(CO)_3Cl$ molecular catalyst through bipyridyl units on the COF backbone (Re-COF). Using the combination of ultrafast spectroscopy and theory, we attributed these differences to the polarized nature of the imine bond that imparts a preferential direction to intramolecular charge transfer (ICT) upon photoexcitation, where the bipyridyl unit acts as an electron acceptor in the forward imine case (f-COF) and as an electron donor in the reverse imine case (r-COF). These interactions ultimately lead the Re-f-COF isomer to function as an efficient CO_2 reduction photocatalyst, while the Re-r-COF isomer shows minimal photocatalytic activity. These findings not only reveal the essential role linker chemistry plays in COF photophysical and photocatalytic properties but also offer a unique opportunity to design photosensitizers that can selectively direct charges.

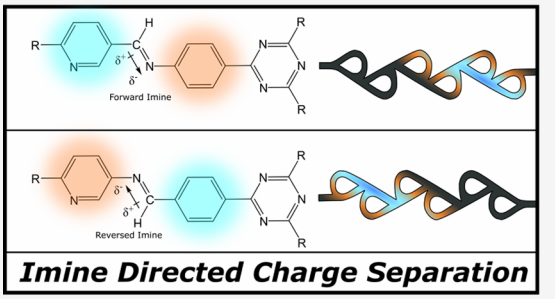

INTRODUCTION

Fuel cells powered by H_2 formed through water splitting (H_2 and O_2), upconverting syn gas (H_2 and CO) derived from CO_2, and affixing H_2 with atmospheric nitrogen as ammonia (N_2 and H_2 to NH_3) represent ideal strategies to sustainably address global resource demands.[1,2] Studying ways to perform these reactions directly using the sun's energy deserves research not only due to its economic possibilities but also because doing so mimics mother nature. Like nature, human-made artificial photosynthesis requires a photocatalytic architecture that can effectively couple a light absorber and a catalyst.[3,4] Two-dimensional (2D) covalent organic frameworks (COFs) are a novel class of crystalline porous materials that are built from aromatic organic monomers linked through covalent bonds. They have been demonstrated as remarkable photocatalytic materials owing to their π-conjugation that often allows absorption of visible light in addition to their inherent porosity, large surface area, and structural diversity.[5−13] Indeed, they have already been recognized as photocatalytic materials in several forms, such as those that incorporate metal catalysts via postsynthetic modification,[14] Z-scheme semiconductor/COF catalysts with covalent heterojunctions,[15] photosensitizers incorporated with cocatalyst,[7,16,17] as well as photocatalysts without metal components.[18] More recently, we have shown the successful integration of $Re(bpy)(CO)_3Cl$ (where bpy is 2,2′-bipyridyl) and $Mn(bpy)(CO)_3Br$ molecular catalyst (MC) into a 2D imine COF featuring a triazine core and bipyridine. We show that these COFs can catalyze CO_2 reduction reactions to form CO with better catalytic activity and durability compared to their corresponding homogeneous counterparts.[4,19]

The imine bond (−C═N−, Schiff base) is widespread among the field of COFs because of its facile formation and reversibility, but there is relatively little known about the photophysical implications of the bond beyond imparting extended π-conjugation between aromatic monomers. Baldwin et al. discovered hints of photophysical differences in two COFs with reversed imine bonds by observing different responses to solvent polarity.[20] Thomas and co-workers dove deeper into the impact of imine reversal reporting changes in the absorption, band alignment, photoconductivity, and

Received: September 26, 2023
Revised: January 16, 2024
Accepted: January 22, 2024

Scheme 1. Synthetic Scheme of (a) f-COF and Re-f-COF and (b) r-COF and Re-r-COF; They Are Built from COF Monomers in which the Amine and Aldehyde Functional Groups Are Switched

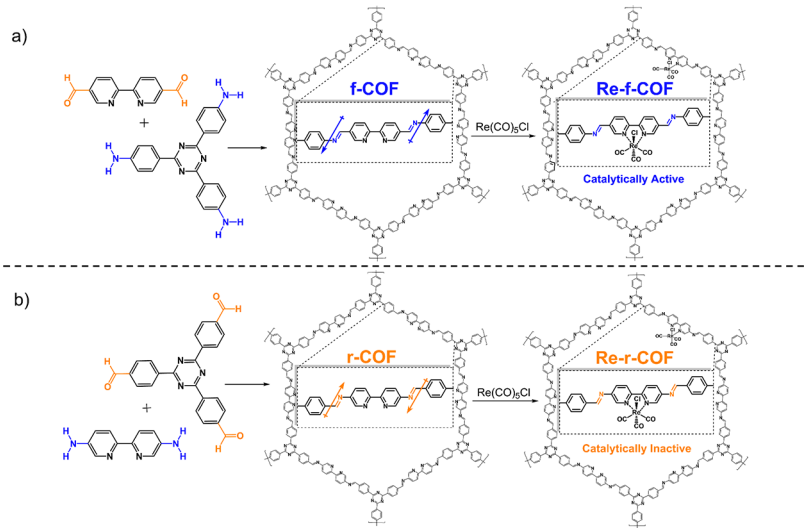

photocatalytic behavior,[21] but the fundamentals for why imine reversal changes these properties remain elusive. A related trend in COF literature is the use of 5,5′-dicarbaldehyde-2,2′-bipyridine (CHO-bpy) as an MC docking site for the formation of photocatalytic COF structures with a variety of comonomers.[22−26] The structural diversity of comonomers with 5,5′-diamino-2,2′-bipyridine (NH_2-bpy), however, is sparse.[27−33] When NH_2-bpy does appear in the literature it is typically stabilized by hydrogen bonding interactions from 1,3,5-triformylphloroglucinol that undergoes keto−enol tautomerization to transform the imine bond into an amine and only a few references exist that polymerize NH_2-bpy without additional hydrogen bonding stabilization.[34,35] Of these, the structures either make use of a tetratopic pyrene monomer that has been shown to be a beneficial crystallization agent,[36] or the crystallinity and porosity of the sample are low.[35] These inherent structural challenges in imine structural isomerism should be recognized as fundamentally important to understand the dynamics of COF formation, and discovering the electronic effects of imine reversal is important to understand how such a ubiquitous linker may affect the performance in COF photocatalysts.

In this work, we begin to fill these needs by reporting in-depth theoretical predictions backed by experimental studies on two imine COF isomers with reversed imine connectivity. We show that the imine direction plays an outsized role in controlling excited state relaxation dynamics whether the COF is bare or coordinated to a Re MC (Re-COF). Photocatalytic CO_2 reduction performance of the Re-COFs, one of which has already been reported,[4] is starkly different, with the reversed imine COF isomer showing no significant activity. We go further to explain this finding by rationalizing that reversing the direction of the imine-linkage changes the behavior of 2,2′-bipyridine, switching it from an electron acceptor in the forward imine COF (f-COF, Scheme 1a) to an electron donor in the reversed imine COF (r-COF, Scheme 1b). This suggests that the direction of imine enforces directionality to intramolecular charge transfer (ICT), an effect we term "*ICT Tesla Valve*" in analogy to diodic one-directional fluidic flow devices.[37] Upon Re incorporation, the impacts of imine reversal to Re/bpy orbital interactions are observable and drastically change the excited state and charge separation pathways. These findings are unprecedented and suggest that when designing COFs for artificial photosynthesis, the linker chemistry in COFs which controls the direction of ICT should be a primary consideration. This may also provide a potential tool in applications where the direction of the ICT is of primary importance.

RESULTS AND DISCUSSION

Synthesis and Structural Characterization of f-COF, Re-f-COF, r-COF, and Re-r-COF. f-COF and Re-f-COF (Scheme 1a) were synthesized following the previously reported method.[4] r-COF (Scheme 1b) is synthesized by adapting a recent synthetic method for colloidal COF formation that uses aniline as a monofunctional polymerization mediator in benzonitrile with a benzoic acid catalyst (details in SI).[38] r-COF is then placed into a teabag, washed by Soxhlet extraction with methanol for 24 h before exchanging with absolute ethanol for critical point drying (CPD, details in SI). Standard characterizations including powder X-ray diffraction (PXRD), Fourier-transformed infrared (FTIR) spectroscopy, ^{13}C−CP-MAS NMR, and diffuse reflectance (DR) spectroscopy are then performed to confirm their structure (details in SI). In addition, small molecular models of f-COF, Re-f-COF, r-COF, and Re-r-COF were synthesized for use as photocatalysis controls (details in SI). We note that we initially attempted to synthesize r-COF by a similar solvothermal method as f-COF by screening for optimal solvent conditions (details in SI, Figures S1−S5), and while this uncovers interesting trends regarding solvent polarity the colloidal method yields r-COF with better porosity and is used in this study.

Figure 1a shows the FTIR spectrum of r-COF, which is featured by an imine (C═N) stretching band at 1620 cm^{-1}, and the attenuation of the −NH_2 band present in NH_2-bpy and the −C═O band present in CHO-TTA. This suggests the formation of the imine bond through the condensation of −NH_2 and −CHO groups. A similar FTIR evolution is observed in the spectrum of f-COF and its monomers (Figure S6), but imine (C═N) stretching is instead found at 1626 cm^{-1}. The ^{13}C−CP-MAS NMR spectrum of r-COF shows a

https://doi.org/10.1021/jacs.3c10627
J. Am. Chem. Soc. XXXX, XXX, XXX−XXX

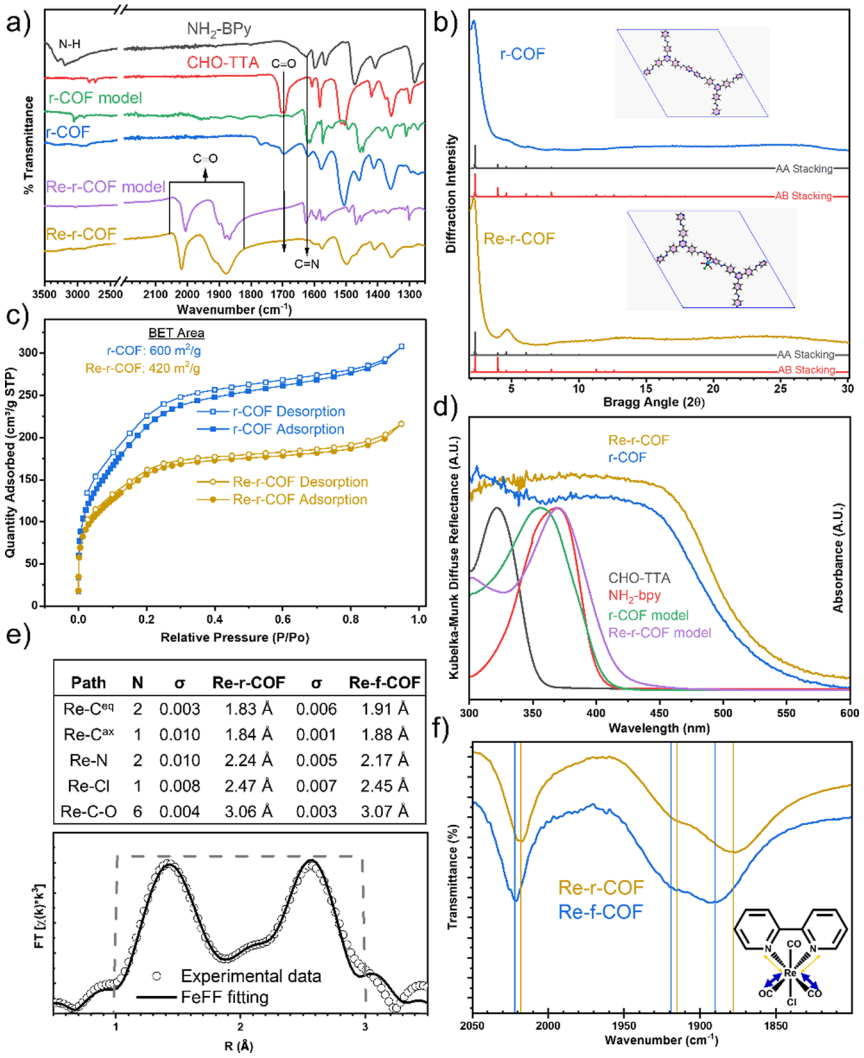

Figure 1. (a) FTIR spectra of r-COF and Re-r-COF. The spectra of monomers and small molecular models are also shown for comparison. (b) Experimental and simulated (AA and AB stacking modes) PXRD patterns of r-COF and Re-r-COF. (c) N_2 adsorption isotherms of r-COF and Re-r-COF with surface areas from BET calculation. (d) UV−visible diffuse reflectance spectra of r-COF and Re-r-COF and the absorption spectra of monomers and small molecular models in acetonitrile solution. (e) EXAFS fitting of Re-r-COF with fitting parameters (top) and R-space fitting (bottom). Note: Re−C−O forward scattering degeneracy of two. (f) FTIR of the (Re)-C≡O stretches in Re-f-COF and Re-r-COF with reference lines drawn through peaks determined by zero crossings of the derivatives (Figure S9).

shoulder at a chemical shift of 159 ppm that we attribute to the imine C (Figure S7). The PXRD patterns (Figure 1b) of r-COF exhibit a relatively intense diffraction peak at 2θ equal to 2.3° but have poorly pronounced higher-order peaks, suggesting a semicrystalline nature. These patterns are similar to that of f-COF (Figure S8), suggesting that r-COF and f-COF have comparable crystallinity and topology. These experimental results are further validated by the computed structure using the density functional tight binding (DFTB)[45−50] optimized unit cell as a lattice model (inset of Figure 1b), where we found that AA stacking is the more probable configuration compared to the AB stacking mode. BET area of r-COF yields r-COF with a BET area of 600 m^2/g (Figure 1c). Because the Kubelka−Munk transformed DR spectra of r-COF (Figure 1d) show broad absorption in the UV−visible regions (>400 nm) where the monomers have negligible absorption, we attribute the absorption at >400 nm to the ICT band, which further supports the formation of r-COF. Overall, the colloidal approach yields similar results by PXRD, FTIR, and DR. The structural effects of imine reversal are not completely clear, but understanding how and why imine structural isomerism affects properties like the imine stretching frequency and porosity is fundamentally important to understanding the dynamics of imine COF formation and deserves further investigation.

Re-r-COF is synthesized by refluxing r-COF with Re$(CO)_5Cl$ in toluene under N_2 protection (Scheme 1b). FTIR spectrum of Re-r-COF (Figure 1a) exhibits three new bands at 1878, 1910, and 2018 cm^{-1}, as determined from the zero crossing of the transmittance derivative (Figure S9). These bands can be assigned to the A'(2), A", and A'(1) stretching modes of C≡O in *fac*-Re(bpy)$(CO)_3Cl$,[39] respectively, which are consistent with the trend of analytic frequencies predicted by DFT (Tables S1 and S2). The PXRD patterns of Re-r-COF show enhanced diffraction peaks with respect to those of r-COF, suggesting that the incorporation of Re to r-COF improves the COF crystallinity (Figure 1b). The reason for this is unknown, but similar trends have been observed upon COF metalation previously.[4,14,29,40] BET analysis of the N_2 isotherm (Figure 1c) of Re-r-COF from the colloidal synthesis

https://doi.org/10.1021/jacs.3c10627
J. Am. Chem. Soc. XXXX, XXX, XXX−XXX

indicates a lower surface area (468 m^2/g) than r-COF which is somewhat expected upon incorporation of Re MC onto the COF backbone and is about 34% that of Re-f-COF (Figure S10). Kubelka−Munk DR spectra of r-COF and Re-r-COF (Figure 1d) indicate that absorption is less red-shifted upon Re incorporation compared with f-COF and Re-f-COF (Figure S11). The incorporation of Re to r-COF to form Re-r-COF is further supported by the X-ray absorption spectrum (XAS) collected at the Re L_3 edge. As shown in Figure 1e, the extended X-ray absorption fine structure (EXAFS) spectrum of Re-r-COF resembles that of $Re(bpy)(CO)_3Cl$ and Re-f-COF (Figure S12) and can be adequately fit by FEFF calculation based on a reported $Re(bpy)(CO)_3Cl$ crystal structure (CCDC Deposition #649892), where Re is coordinated by three C (C≡O), two N (bpy), and one Cl. This unambiguously confirms the presence of *fac*-$Re(bpy)(CO)_3Cl$ and supports that Re was incorporated into r-COF through bipyridine in Re-r-COF.[39,41−43] The fitting results (top panel in Figure 1e) indicate a decrease in the Re−C bond length in Re-r-COF (1.83 Å equatorial and 1.84 Å axial) compared with those in Re-f-COF (1.91 Å equatorial and 1.88 Å axial). These bond reductions in Re-r-COF coincide with the elongation of Re−N (2.24 Å) and Re−Cl (2.47 Å) bonds, as opposed to those in Re-f-COF (2.17 Å for Re−N and 2.45 Å for Re−Cl). However, Re → C → O forward scatterings exhibit only minor changes, where it is 3.06 Å in Re-r-COF and 3.07 Å in Re-f-COF. This results in a net increase of 0.07 and 0.03 Å in the equatorial and axial C≡O bond lengths, respectively.

Differences in the EXAFS results between Re-f-COF and Re-r-COF can be attributed to π back-bonding from Re d-orbitals (with π symmetry) to antibonding C≡O (π^*) molecular orbitals. Re($d\pi$) → C≡O (π^*) back bonding is stronger in Re-r-COF and thus a stronger and shorter Re−C bond but a weaker and longer C≡O bond than those in Re-f-COF. Note that a larger C≡O net elongation is observed in equatorial C≡O than in axial C≡O, suggesting that the impact of imine reversal on π back-bonding is more effective in the former than the latter. Further support of these findings arises from the FTIR spectra, where C≡O stretching modes in Re-r-COF have a lower frequency (1878, 1912, and 2018 cm^{-1}) than those in Re-f-COF (1890, 1910, and 2021 cm^{-1}) due to increased Re($d\pi$) → C≡O (π^*) back bonding in the former (Figure 1f). These results together suggest that the imine direction effectively impacts the π-acceptor characteristics of the bipyridine in both f-COF and r-COF, where Re($d\pi$) → bipyridine(π^*) back-bonding has an inverse relationship with Re($d\pi$) → C≡O(π^*) back-bonding.

Reversal of the Imine Direction Impacts Ground-State Transitions of COFs. To understand how imine direction impacts the electronic transitions and photophysical properties of f-COF and r-COF, we evaluate the electronic correlation between the four fragments (i.e., triazine, phenylene, bipyridine, and imine, Figure 2a) by performing time-dependent DFT (TDDFT)[53−58] calculations on the edge units (Figure 2a), followed by transition density matrix (TDM) analysis (with details in Supporting Information).[59] The selection of the four fragments-triazine, phenylene, bipyridine, and imine- is based on the rationale that they play important roles in ICT and are essential for TDM analysis. As shown in the left panel of Figure 2b, the matrix elements in the electron correlation plot of f-COF suggest that electron transfer from phenylene to both imine and bipyridine contributes to ICT. In contrast, the electron correlation plot of r-COF which has a

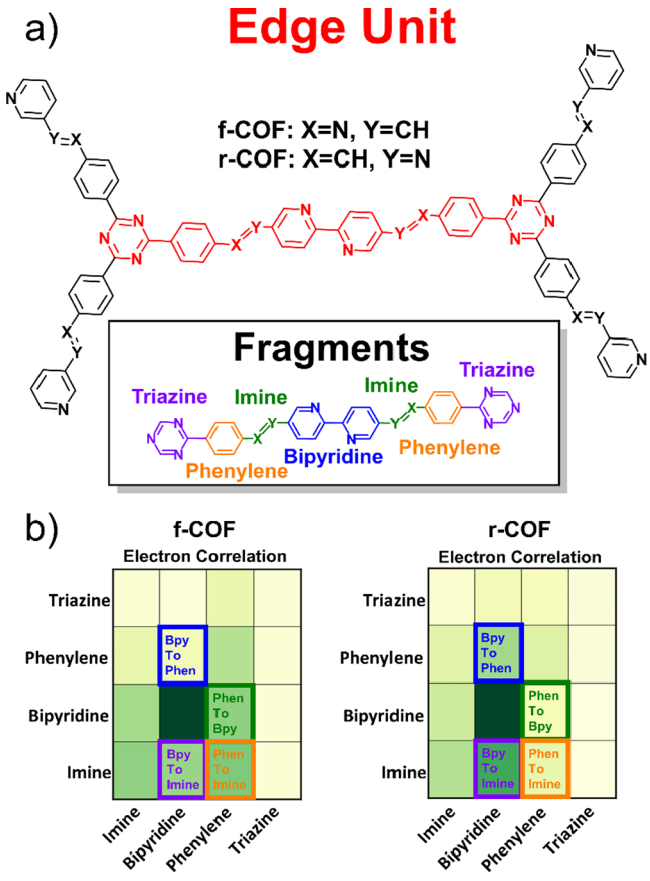

Figure 2. (a) Molecular structure of the edge unit of f-COF and r-COF and the fragments chosen for TDM analysis. (b) Electron correlation plots of the allowed S_1 transition produced by TDM analysis; f-COF (left) and r-COF (right). The *X*-axis represents the fragment from which the electron density originates, while the *Y*-axis denotes the fragment where the electron density ends up. Darker colors correspond to a higher degree of correlation among the fragments. Outlines show the key differences pertaining to ICT.

reversal imine direction (right panel in Figure 2b) indicates the opposite behavior, where ICT has a contribution from hole transfer from phenylene to bipyridine and imine, i.e., reversing the ICT direction. The electron correlation plot illustrates this by showing more correlation (darker green) in the bipyridine → imine and bipyridine → phenylene matrix elements, and less correlation (lighter green) in the phenylene → imine and phenylene → bipyridine matrix elements of r-COF and f-COF, respectively. This finding has an analogy to one-way fluidic valves (e.g., "*Tesla Valve*"), highlighting the crucial impact the imine direction has on ICT in imine-based COFs.[37]

Reversal of Imine Direction Impacts the Excited State Dynamics of COFs. The excited state (ES) dynamics of f-COF and r-COF are examined using femtosecond transient absorption (fs-TA) spectroscopy. ES properties are measured by pumping f-COF and r-COF samples with a 400 nm 150 μJ laser and using delayed visible light pulses to generate the ES spectra. A distinct excited state absorption (ESA) peak at 500 nm is observed in the fs-TA spectrum of f-COF at 500 fs and persists until 1 ns (Figure 3a). The presence of a clearly defined peak indicates that ESA occurs from ground-state electrons being promoted to a relatively localized electronic ES. Notably, while this peak is no longer observable past 1 ns, a broad positive feature persists, suggesting an underlying state is

https://doi.org/10.1021/jacs.3c10627
J. Am. Chem. Soc. XXXX, XXX, XXX−XXX

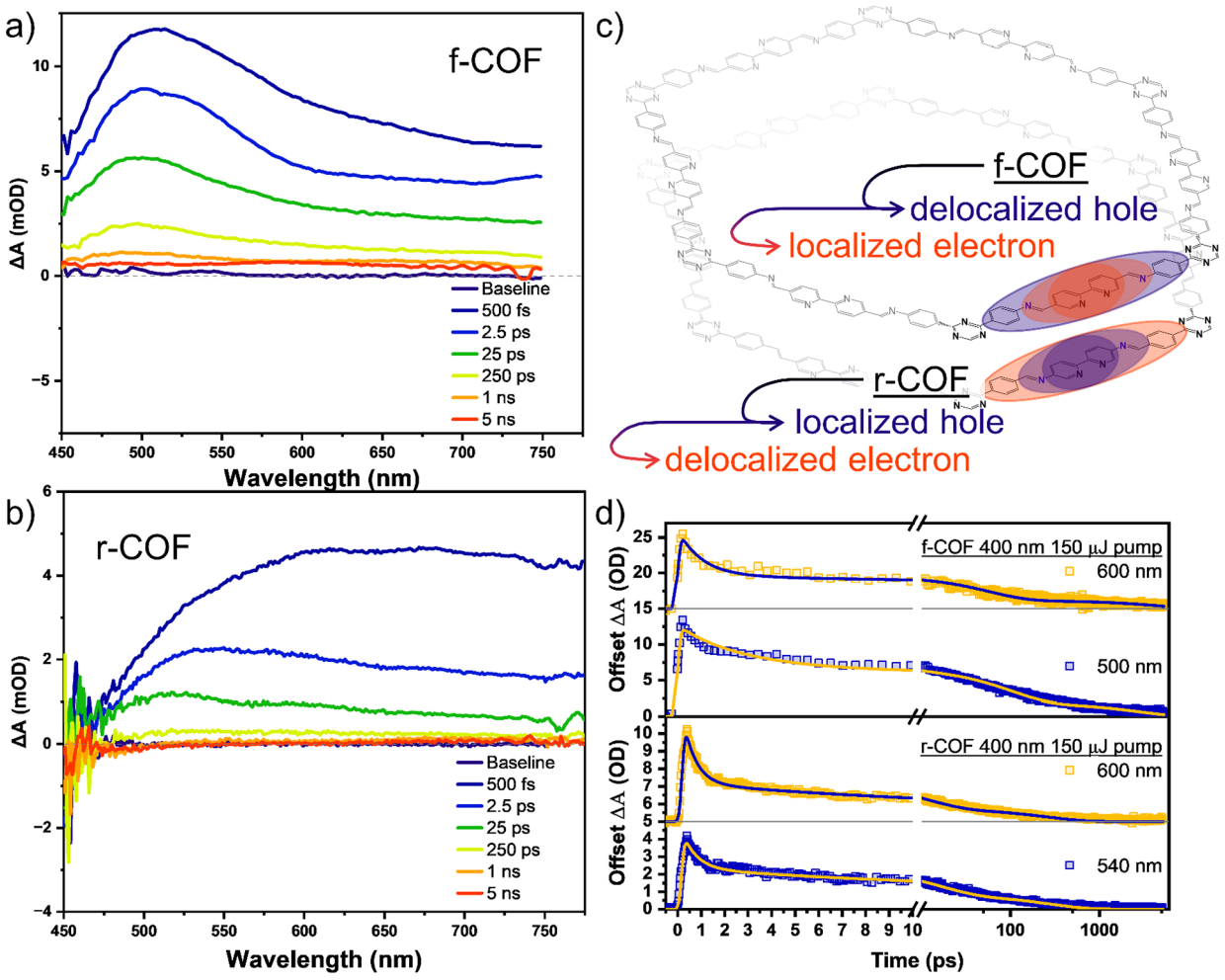

Figure 3. (a) fs-TA time slices of f-COF. (b) Fs-TA time slices of r-COF. (c) Pictorial scheme of exciton localization in the f-COF and r-COF. (d) fs-TA kinetic traces of f-COF (top) and r-COF (bottom) at various wavelengths.

present. TDM analysis (vide supra) shows that the exciton generated by the pump laser should localize electron density primarily at the bipyridine. In this case, the hole density is delocalized, overlapping the bipyridine, imine, and phenylene fragments. In contrast, r-COF seems to initially populate a rather electronically delocalized ES with a broad, featureless ESA profile that returns to the ground state (GS) within the fs-TA time window (Figure 3b). ESA in r-COF initially extends across the visible spectrum and shows no prominent peaks, but as time passes, a peak is dynamically evident; the peak maximum arises at 525 nm in 2.5 ps and then migrates to 500 nm in 25 ps. Peak formation and migration represent exciton self-trapping of carriers, in this case, electrons, that cannot escape Coulombic attraction to holes in the low dielectric environment of the framework.[51,52] Thus, the initially delocalized state localizes relatively quickly before exciton recombination brings the system back to the GS by 1 ns.

Theoretical and experimental results are thus in accordance with each other, allowing for summarization of the results in Figure 3c. f-COF initially generates a delocalized hole with localized electron while r-COF generates the opposite: a localized hole with delocalized electron. Figure 3d shows the kinetic traces of f-COF (top) and r-COF (bottom) that are fit by a finite three-component exponential decay for both COFs. It is difficult to definitively interpret what processes the time components correspond to without specific further study, but they are likely due to some combination of vibrational relaxation, exciton self-trapping, and recombination. The noticeable features of the fitting components (Table S3) are that the first component in r-COF is faster and makes up a larger portion of the overall relaxation than the first component in f-COF. Fast processes in this time range could correspond to structural relaxation and a larger proportion suggests r-COF undergoes more structural distortion than f-COF. Interestingly, the 540 and 500 nm probe in r-COF and f-COF, respectively, have similar proportions of the overall relaxation.

Reversal of the Imine Direction Impacts Ground-State Transitions in Re-COFs. The impact of the imine direction on the electronic structure and energetics of Re-f-COF and Re-r-COF is also assessed. The lowest energy transition with appreciable oscillator strength (GS → S_4, Tables S4 and S5), which should be the main absorbance peak in the visible portion of the DR spectrum for both Re-COFs, is 0.13 eV higher in energy in Re-r-COF than Re-f-COF. This absorption energy difference is reflected in the measured DR spectra of Re-COFs where Re-r-COF is centered around 450 nm (Figure 1d) and Re-f-COF is centered around 475 nm (Figure S11). Natural transition orbitals (NTOs, Figure 4a)[66] of this GS → S_4 transition in Re-f-COF indicate the presence of a hole particle centered on the COF and an electron particle with mixed Re/f-COF characteristics. This may suggest the presence of a small degree of ligand-to-metal charge transfer

https://doi.org/10.1021/jacs.3c10627
J. Am. Chem. Soc. XXXX, XXX, XXX−XXX

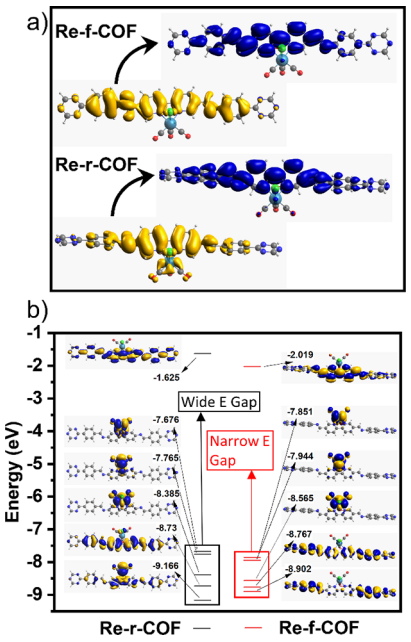

Figure 4. (a) Visualization of the NTO corresponding to the lowest allowed singlet transition of Re-f-COF (S_4, f = 1.86) and Re-r-COF (S_4, f = 1.96) at the S_0 geometry. (b) Frontier orbital diagram of Re-f-COF and Re-r-COF at the S_0 geometry.

(LMCT) immediately following excitation but is primarily intraligand charge transfer (ILCT) in nature. In contrast, the Re-r-COF NTO of the S_4 transition shows a hole particle with mixed Re/r-COF orbital contributions (Figure 4a, bottom), suggesting some degree of metal-to-ligand charge transfer (MLCT) nature that is typically observed in Re(bpy)-$(CO)_3Cl$.[42] Frontier orbitals (Figure 4b) illustrate the effect of imine reversal on the Re/COF energetic overlap in Re-COFs. In Re-r-COF the occupied MOs localizing electron density on Re (HOMO, HOMO−1, HOMO−2) and those localized on COF (HOMO−3) are energetically separated relative to those of Re-f-COF. This disparity is attributed to that Re-r-COF has a relatively electron-rich bipyridine ground state, which leads to energy lowering that inhibits the mixing of Re($d\pi$) and bipyridine(π^*) orbitals. This is consistent with the results from XAS and FTIR spectroscopy (Figure 1e,f) and our DFT prediction (Tables S1 and S2), where Re-r-COF shows stronger Re($d\pi$) → C≡O (π^*) but weaker Re($d\pi$) → bipyridine(π^*) back bonding and lower C≡O stretching frequencies.

Reversing the Imine Direction Impacts the ES and CS Dynamics of Re-COFs. The impact of imine reversal on the ES and charge separation (CS) dynamics of Re-COFs is examined by both femtosecond (fs-TA) and nanosecond (ns-TA) transient absorption spectroscopy. Immediately following 400 nm excitation, the fs-TA spectra of Re-f-COF (top panel in Figure 5a) show a negative feature at ∼470 nm corresponding to the ground state bleach (GSB), a broad positive feature (>500 nm) that can be attributed to ESA, and an isosbestic point at 500 nm. At early time (<250 ps), the isosbestic point shows a bathochromic shift (by ∼25 nm), which is simultaneously accompanied by the broadening of GSB, suggesting that the system undergoes relaxation to form a new intermediate state. Re-r-COF has significantly different initial fs-TA spectra from Re-f-COF; displaying a bimodal ESA across the entire spectral window with peaks at 630 and 525

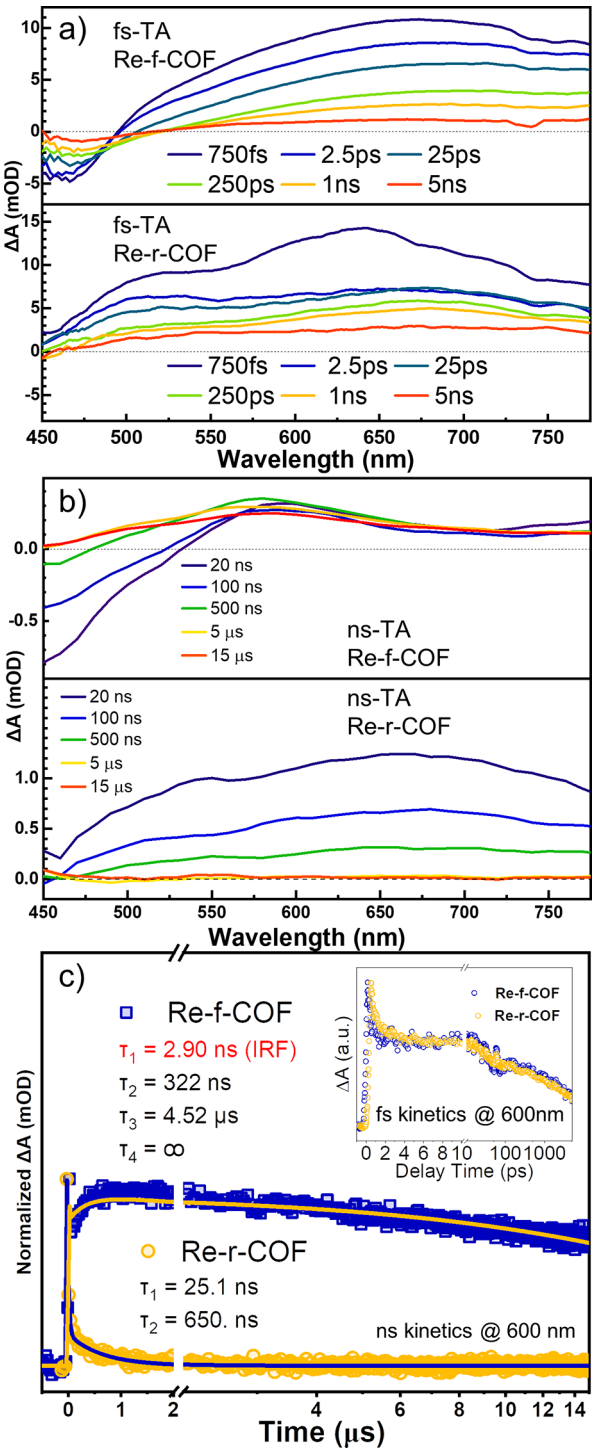

Figure 5. (a) Femtosecond TA spectra of Re-f-COF (top) and Re-r-COF (bottom) upon 400 nm excitation. (b) Nanosecond TA spectra of Re-f-COF (top) and Re-r-COF (bottom) after 355 nm excitation. (c) Comparison of kinetic traces at 600 nm between Re-f-COF and Re-r-COF from nanosecond TA spectra. The inset shows the comparison of the kinetics from fs-TA.

nm, and no observable GSB. Spectral evolution also occurs within 250 ps, in the form of a red-shifting from the 630 nm peak to 675 nm, suggesting the relaxation of an intermediate excited state in Re-r-COF. By the end of the fs-TA time window, the profiles of Re-f-COF and Re-r-COF somewhat resemble one another, except for the persistent GSB in Re-f-

https://doi.org/10.1021/jacs.3c10627
J. Am. Chem. Soc. XXXX, XXX, XXX−XXX

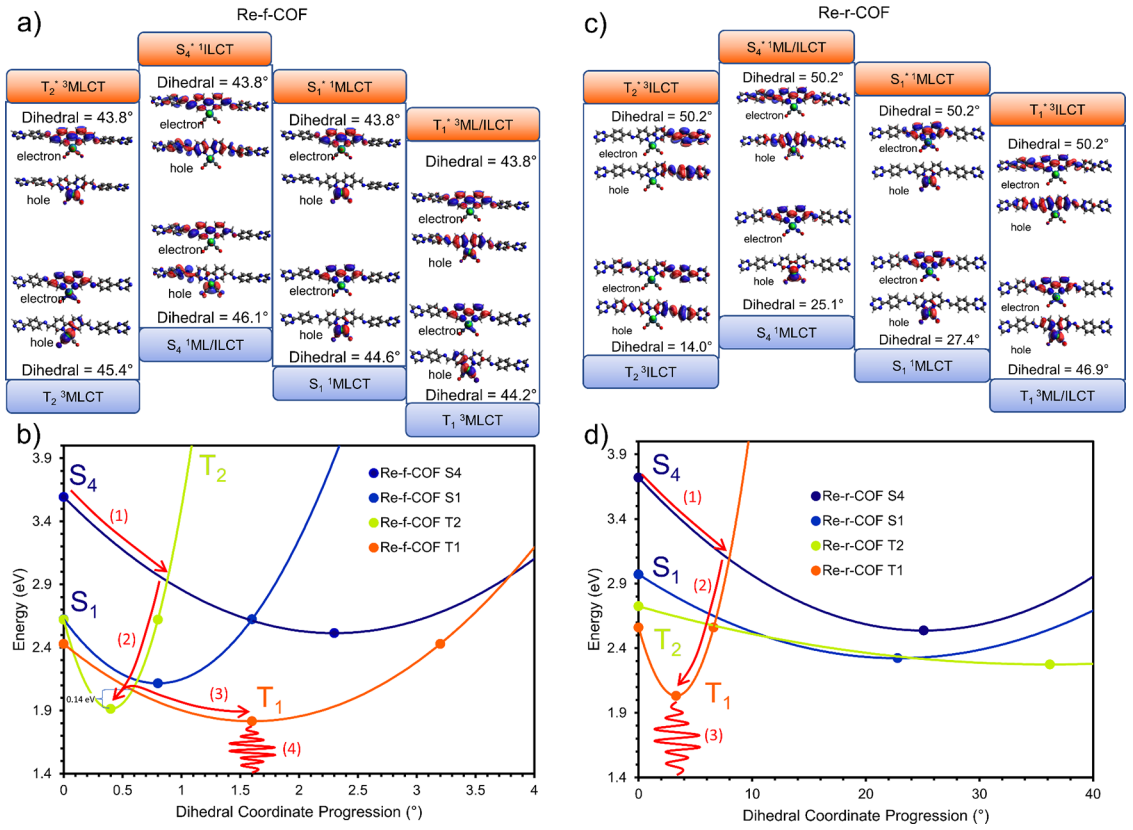

Figure 6. (a) TDDFT predicted NTOs of excited states at the S_0 geometry (top) and optimized geometry (bottom) of Re-f-COF. (b) Excited state potential energy surfaces of Re-f-COF as a function of the phenyl-bipyridine dihedral angle assuming parabolic surfaces. (c) TDDFT predicted NTOs of excited states at the S_0 geometry (top) and optimized geometry (bottom) of Re-r-COF. (d) Excited state potential energy surfaces of Re-r-COF as a function of the phenyl-bipyridine dihedral angle assuming parabolic surfaces.

COF. At the beginning of the ns-TA window, Re-f-COF (Figure 5b, top panel) still exhibits a GSB toward the blue and an ESA centered at 600 nm, resembling the signature at the end of its fs-TA. Prominent spectral evolution takes place where the GSB decays into ESA by 5 μs then the whole ESA persists past 15 μs. After recovery of the GSB, the broad ESA appears relatively unchanged, suggesting the recovery or interconversion of an intermediate species in Re-f-COF on a ns time scale. In contrast, the ns-TA spectra of Re-r-COF (Figure 5b, bottom panel) have a single broad ESA spectral feature with maximal ΔA at 675 nm that decays monotonically back to the ground state within 15 μs.

The kinetic traces of the visible TA measurements are shown in Figure 5c. On a femtosecond time scale, the decay of the normalized 600 nm signal is comparable between the Re-COFs (inset of Figure 5c), suggesting the broad ESA corresponds to the population of a similar excited state. The GSB in Re-f-COF recovers within 5 μs, and the ESA grows, indicating that it is either overlapped with GSB or that a new state is populated (Figure 5c). Regardless, the presence of an ES population beyond our ns-TA window (15 μs) suggests the presence of an exceptionally long-lived ES in Re-f-COF. Indeed, efforts to determine its full lifetime were unsuccessful since there is still a substantial signal remaining even after 4 ms. This is in stark contrast to the ESA lifetime of Re-r-COF, which completely decays within 6 μs. Since the ESA of r-COF is completely decayed by the end of the fs-TA time window we can rule out r-COF exciton recombination from possible ESA contributions in ns-TA.

To further develop a hypothesis for Re-f-COF having a longer-lived excited state we turn to TDDFT to help describe differences the Re-COFs have in their ^{3}MLCT manifold.[60−65] Starting from the GS geometry, the transitions predicted by TDDFT can be inspected by generating the NTOs (top of Figure 6a,b). Re-f-COF has an optically allowed vertical transition to the S_4 state which has ^{1}ILCT character (f = 1.86, vide supra). The optically forbidden (f = 0.00) GS → S_1 transition has ^{1}MLCT character, GS → T_2 is ^{3}MLCT, and GS → T_1 is mixed ^{3}ML/ILCT. Re-r-COF has a mixed ^{1}ML/ILCT character for its optically allowed GS → S_4 transition (f = 1.96), ^{1}MLCT for GS → S_1, and ^{3}ILCT for GS → T_1 and GS → T_2.

TDDFT optimization of excited states is performed under the constraint that the two triazines of the edge fragments remain planar to replicate the bulk environment of the COFs (Figure 2a). At their respective optimized geometries, the S_4 state of Re-f-COF takes on mixed ^{1}ML/ILCT character, the S_1 state remains ^{1}MLCT, while T_2 and T_1 both remain ^{3}MLCT. In Re-r-COF the S_4 state becomes ^{1}MLCT, S_1 remains ^{1}MLCT, T_2 remains ^{3}ILCT, and T_1 becomes mixed ^{3}ML/ILCT. The relationship between state identity and dihedral angle is best represented by plotting potential energy surfaces under the assumption they are parabolic (Figure 6c,d). In Re-f-COF the small dihedral progressions should allow for a variety of pathways through the ES manifold, but the most prominent is outlined in three steps (Figure 6c). The first step involves relaxation of the S_4 state until ISC to T_2 occurs; ISC has been suggested by studies on Re(bpy) complexes to occur quickly.[44]

https://doi.org/10.1021/jacs.3c10627
J. Am. Chem. Soc. XXXX, XXX, XXX−XXX

Next, the system relaxes along the T_2 potential to its energetic minima; we infer that crossing to the T_1 state can be reasonably well avoided due to the mixed ^{3}ML/ILCT character of the latter which would require hole transfer to f-COF. At the T_2 minima, thermal equilibrium with the T_1 state ($\Delta G^{\ddagger} = 0.14$ eV under parabolic PES assumption) can be established. Finally, once the T_1 minima has been reached, relaxation back to the GS can take place. Re-r-COF has a larger bipyridine-phenylene dihedral progression than Re-f-COF, but notably, the dihedral progression for the T_1 relaxation in Re-r-COF is much smaller than those in its other investigated transitions. The dihedral progression of Re-r-COF proceeds toward planarization and is evidently due to the delocalization of electron density in the excited state, as observed in fs-TA measurements of r-COF, which may be key to its rapid excited state deactivation. The generally large dihedral progression and energetic isolation of the S_4 state offer fewer pathways through the ES manifold (Figure 6d). The likely pathway would follow relaxation along the S_4 potential until crossing onto the T_1 potential where the excitation resides until relaxation back to the GS can occur.

Combining the findings from TA spectroscopy and TDDFT computation, we propose a hypothesis on the ES relaxation dynamics that can well explain the experimental data we have observed. The pump initially excites Re coordinated sites from GS to ^{1}ILCT in Re-f-COF or mixed ^{1}ML/ILCT in Re-r-COF. Conversely, excitons at bare sites underlie ^{1}MLCT → ^{3}MLCT at Re coordinated sites and recombine within 5 ns. Both Re-COFs initially undergo intersystem crossing to ^{3}MLCT states, but this lifetime is decreased in Re-r-COF due to more metal−ligand mixing in the T_1 than Re-f-COF that experiences slow interconversion of the T_2 state to the T_1. This interconversion is observable by the recovery of GSB into ESA in ns-TA by shifting dσ occupation at 10 ns. Re−N bond distances support shifting occupation into dσ orbitals. At T_2 the Re−N(1) and the Re−N(2) distance is 2.19 and 2.09 Å, respectively, while at T_1 Re−N(1) is 2.17 Å and Re−N(2) is 2.14 Å. This interpretation suggests that the T_2 state is being probed at 10 ns before significant interconversion to T_1 can take place.

Impact of the Imine Direction on Photocatalytic Performance. Our fundamental photophysical studies discussed above suggest a distinct difference of electronic structure and ICT due to imine reversal between COFs and Re-COFs. Our next step is to evaluate whether imine reversal in Re-COFs impacts their catalytic performance for light-driven CO_2 reduction to generate CO, and how the photophysical properties of COFs and Re-COFs are correlated with their catalytic functions. The photocatalytic CO_2 reduction reactions are conducted in an 11 mL vial containing 3.0 mL of CH_3CN, 0.2 mL of triethanolamine (TEOA), and 1.0 mg of Re-COF. The headspace of the reaction vial was sampled by removing 200 μL with an airtight syringe and manually loading an Agilent 490 Micro Gas Chromatograph (GC) equipped with a thermal conductivity detector. Control studies were performed without catalyst, without CO_2, with $^{13}CO_2$, without light, and with TEA or H_2O as electron donors (Figure S13). Additionally, model compounds of the Re-COFs were synthesized by performing Schiff base condensation between CHO-bpy with aniline and NH_2-bpy with benzaldehyde followed by refluxing with $Re(CO)_5Cl$ in toluene (see Supporting Information for details). The reaction vial was purged with CO_2 for 15 min and a Xe lamp with a cut off filter (>420 nm) was used to illuminate the sample. In addition, a one-foot water filter is placed after the Xe lamp to remove IR light, which simulates solar radiation passing through water vapor in the atmosphere. The Re mass percent in Re-COFs is determined by ICP-MS, which is 6.2% Re in Re-f-COF and 7.4% Re in Re-r-COF (Figure S14). Under these experimental conditions, Re-f-COF can produce 6.3 ± 1.2 mmol CO per gram of the Re-f-COF catalyst after 8 h (equivalent to 4.5 μmol per unit surface area). In contrast, Re-r-COF can only generate 0.30 ± 0.05 mmol CO per gram of the Re-r-COF catalyst in the same duration (0.5 μmol per unit surface area). These results were also reflected by model systems of Re-f-COF and Re-r-COF that also showed that reversal of the imine linker significantly hinders or entirely shuts off CO_2 photoreduction (Figure 7b). We note that while the performance of

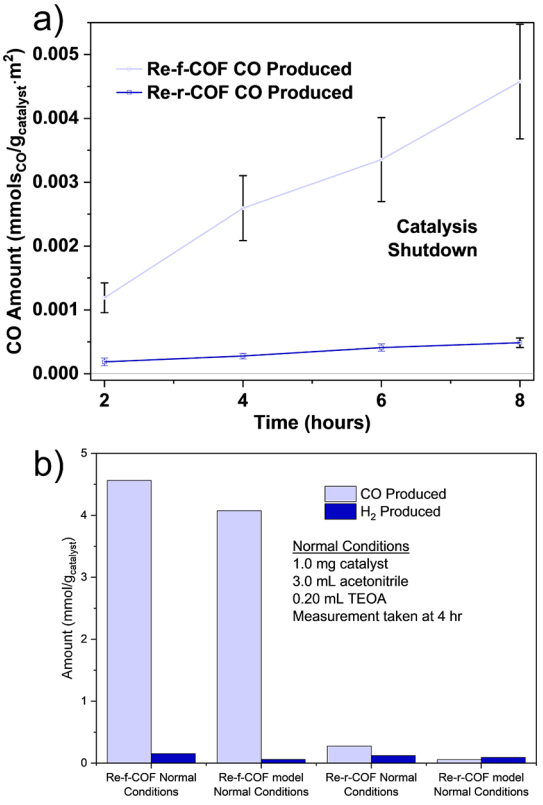

Figure 7. (a) Time profile of CO production from CO_2 by Re-f-COF and Re-r-COF per gram of COF catalyst and normalized to the unit surface area. Error bars represent 90% CI (n = 3). (b) Control experiments performed on Re-f-COF and Re-r-COF models where the catalyst loading is 1 mg Re-COF (~6−7 mass % Re) or 1 mg Re-COF model (27.9 mass % Re).

the model systems is similar to the Re-COF systems, the Re loading in the Re-COFs is significantly lower since the $g_{catalyst}$ is measured as gross mass. After a reaction vial was purged with isotopically labeled $^{13}CO_2$, a tiny portion of ^{12}CO could be detected by GC-MS for both Re-f-COF and Re-r-COF photocatalysts, suggesting a portion of the CO detected may be due to decomposition of the catalyst (Figure S15). Importantly, the integrated peak area of the ^{12}CO response is similar between Re-f-COF and Re-r-COF (Figure S15b,f), but the proportion of ^{13}CO produced by Re-f-COF is much higher. These findings suggest that imine reversal from Re-f-COF to Re-r-COF significantly reduces the catalytic activity for CO_2 → CO photoreduction. Characterizing the Re-COFs

https://doi.org/10.1021/jacs.3c10627
J. Am. Chem. Soc. XXXX, XXX, XXX−XXX

after the photocatalytic reaction by FTIR (Figure S16) shows that the Re center in each is coordinated by acetonitrile and that the imine bond at 1620−1626 cm^{-1} appears to be protonated, corresponding to a new peak at 1603 cm^{-1}.

CONCLUSIONS

In summary, we report two imine COF isomers with reversed imine connectivity (f-COF and r-COF), which demonstrated distinct photophysical properties and photocatalytic performance for light-driven CO_2 reduction to generate CO after incorporating a $Re(bpy)(CO)_3Cl$ molecular catalyst to the COF backbone. Theory-led investigations are supported by experimental results from ultrafast transient absorption spectroscopy that show imine linkers impart a preferential direction to ICT, where bipyridine in f-COF built from CHO-bpy and NH_2-TTA is an electron acceptor whereas it acts as an electron donor in r-COF composed of CHO-TTA and NH_2-bpy. The reversal of imine also causes a switch in exciton localization in bare-COFs, affects the coordination of $Re(bpy)(CO)_3Cl$ to the COF, and promotes different charge separation mechanisms in Re-COFs, where a significantly more prolonged excited state was observed in Re-f-COF than in Re-r-COF. These properties ultimately result in the Re-f-COF isomer acting as an effective photocatalyst for CO_2 reduction, whereas the Re-r-COF isomer exhibits negligible photocatalytic activity. These discoveries not only suggest that the chemistry of linker should be the primary focus when developing imine-linked COFs for photocatalytic applications but also offer a new approach for controlling the charge transfer direction in COFs, which may open a new avenue for their applications in solar energy conversion.

ASSOCIATED CONTENT

Supporting Information

The Supporting Information is available free of charge at https://pubs.acs.org/doi/10.1021/jacs.3c10627.

Synthesis of COFs, standard characterization, TA experiments, XRD patterns, NMR, mass spectra, single crystal data, BET results, XAS spectra, computational results, fitting parameters for TA and XAS results, and catalytic results (PDF)

Accession Codes

CCDC 2311631−2311632 contain the supplementary crystallographic data for this paper. These data can be obtained free of charge via www.ccdc.cam.ac.uk/data_request/cif, or by emailing data_request@ccdc.cam.ac.uk, or by contacting The Cambridge Crystallographic Data Centre, 12 Union Road, Cambridge CB2 1EZ, UK; fax: +44 1223 336033.

AUTHOR INFORMATION

Corresponding Author

Jier Huang − *Department of Chemistry, Marquette University, Milwaukee, Wisconsin 53233, United States; Department of Chemistry, Boston College, Chestnut Hill, Massachusetts 02467, United States;* orcid.org/0000-0002-2885-5786; Email: jier.huang@bc.edu

Authors

Daniel H. Streater − *Department of Chemistry, Marquette University, Milwaukee, Wisconsin 53233, United States*

Eric R. Kennehan − *Magnitude Instruments, State College, Pennsylvania 16803, United States*

Denan Wang − *Department of Chemistry, Boston College, Chestnut Hill, Massachusetts 02467, United States;* orcid.org/0000-0003-3603-6788

Christian Fiankor − *Department of Chemistry, University of Nebraska-Lincoln, Lincoln, Nebraska 68588, United States;* orcid.org/0009-0000-5299-8835

Liangji Chen − *Department of Chemistry, Boston College, Chestnut Hill, Massachusetts 02467, United States*

Chongqing Yang − *Molecular Foundry, Lawrence Berkeley National Laboratory, Berkeley, California 94720, United States*

Bo Li − *Department of Chemistry, Boston College, Chestnut Hill, Massachusetts 02467, United States*

Daohua Liu − *Department of Chemistry, Wayne State University, Detroit, Michigan 48202, United States*

Faysal Ibrahim − *Department of Chemistry, University of Wisconsin-Madison, Madison, Wisconsin 53706, United States;* orcid.org/0000-0003-3354-8104

Ive Hermans − *Department of Chemistry, University of Wisconsin-Madison, Madison, Wisconsin 53706, United States; Department of Chemical and Biological Engineering, University of Wisconsin−Madison, Madison, Wisconsin 53706, United States;* orcid.org/0000-0001-6228-9928

Kevin L. Kohlstedt − *Department of Chemistry, Northwestern University, Evanston, Illinois 60208, United States;* orcid.org/0000-0001-8045-0930

Long Luo − *Department of Chemistry, Wayne State University, Detroit, Michigan 48202, United States;* orcid.org/0000-0001-5771-6892

Jian Zhang − *Molecular Foundry, Lawrence Berkeley National Laboratory, Berkeley, California 94720, United States;* orcid.org/0000-0003-0274-0814

Complete contact information is available at: https://pubs.acs.org/10.1021/jacs.3c10627

Notes

The authors declare no competing financial interest.

ACKNOWLEDGMENTS

This research was supported by the U.S. Department of Energy, Office of Science, Office of Basic Energy Sciences, under Award No. DE-SC0024049. This work used high-performance computational facilities supported by National Science Foundation grant numbers ACI-1548562 and CNS-1828649. The use of X-ray absorption spectroscopy at Advanced Photon Source, Beamline 12-BM, in Argonne National Laboratory was supported by the U.S. Department of Energy, Office of Science, Office of Basic Energy Sciences, under Award No. DE-AC02-06CH11357. The use of single crystal X-ray diffractometer is supported by NIH, under Award No. S10OD030360. Work at the Molecular Foundry was supported by the Office of Science, Office of Basic Energy Sciences, of the U.S. Department of Energy under Contract No. DE-AC02-05CH11231. This work was adapted from the dissertation of D.H.S.

REFERENCES

(1) Ashford, D. L.; Gish, M. K.; Vannucci, A. K.; Brennaman, M. K.; Templeton, J. L.; Papanikolas, J. M.; Meyer, T. J. Molecular Chromophore−Catalyst Assemblies for Solar Fuel Applications. *Chem. Rev.* **2015**, *115* (23), 13006−13049.

(2) Lewis, N. S. Introduction: Solar Energy Conversion. *Chem. Rev.* **2015**, *115* (23), 12631−12632.

(3) Pan, Q.; Abdellah, M.; Cao, Y.; Lin, W.; Liu, Y.; Meng, J.; Zhou, Q.; Zhao, Q.; Yan, X.; Li, Z.; Cui, H.; Cao, H.; Fang, W.; Tanner, D. A.; Abdel-Hafiez, M.; Zhou, Y.; Pullerits, T.; Canton, S. E.; Xu, H.; Zheng, K. Ultrafast Charge Transfer Dynamics in 2D Covalent Organic Frameworks/Re-Complex Hybrid Photocatalyst. *Nat. Commun.* **2022**, *13* (1), 845.
(4) Yang, S.; Hu, W.; Zhang, X.; He, P.; Pattengale, B.; Liu, C.; Cendejas, M.; Hermans, I.; Zhang, X.; Zhang, J.; Huang, J. 2D Covalent Organic Frameworks as Intrinsic Photocatalysts for Visible Light-Driven CO2 Reduction. *J. Am. Chem. Soc.* **2018**, *140* (44), 14614−14618.
(5) Diercks, C. S.; Yaghi, O. M. The Atom, the Molecule, and the Covalent Organic Framework. *Science* **2017**, *355* (6328), No. eaal1585.
(6) Huang, N.; Wang, P.; Jiang, D. Covalent Organic Frameworks: A Materials Platform for Structural and Functional Designs. *Nat. Rev. Mater.* **2016**, *1* (10), 16068.
(7) Vyas, V. S.; Haase, F.; Stegbauer, L.; Savasci, G.; Podjaski, F.; Ochsenfeld, C.; Lotsch, B. A Tunable Azine Covalent Organic Framework Platform for Visible Light-Induced Hydrogen Generation. *Nat. Commun.* **2015**, *6*, 8508.
(8) Bunck, D. N.; Dichtel, W. R. Postsynthetic Functionalization of 3D Covalent Organic Frameworks. *Chem. Commun.* **2013**, *49* (24), 2457−2459.
(9) Waller, P. J.; Lyle, S. J.; Osborn Popp, T. M.; Diercks, C. S.; Reimer, J. A.; Yaghi, O. M. Chemical Conversion of Linkages in Covalent Organic Frameworks. *J. Am. Chem. Soc.* **2016**, *138* (48), 15519−15522.
(10) Kandambeth, S.; Dey, K.; Banerjee, R. Covalent Organic Frameworks: Chemistry beyond the Structure. *J. Am. Chem. Soc.* **2019**, *141* (5), 1807−1822.
(11) Zhao, W.; Xia, L.; Liu, X. Covalent Organic Frameworks (COFs): Perspectives of Industrialization. *CrystEngComm* **2018**, *20* (12), 1613−1634.
(12) Vazquez-Molina, D. A.; Mohammad-Pour, G. S.; Lee, C.; Logan, M. W.; Duan, X.; Harper, J. K.; Uribe-Romo, F. J. Mechanically Shaped Two-Dimensional Covalent Organic Frameworks Reveal Crystallographic Alignment and Fast Li-Ion Conductivity. *J. Am. Chem. Soc.* **2016**, *138* (31), 9767−9770.
(13) Li, X.; Zhang, C.; Cai, S.; Lei, X.; Altoe, V.; Hong, F.; Urban, J. J.; Ciston, J.; Chan, E. M.; Liu, Y. Facile Transformation of Imine Covalent Organic Frameworks into Ultrastable Crystalline Porous Aromatic Frameworks. *Nat. Commun.* **2018**, *9* (1), 2998.
(14) Fu, Z.; Wang, X.; Gardner, A. M.; Wang, X.; Chong, S. Y.; Neri, G.; Cowan, A. J.; Liu, L.; Li, X.; Vogel, A.; Clowes, R.; Bilton, M.; Chen, L.; Sprick, R. S.; Cooper, A. I. A Stable Covalent Organic Framework for Photocatalytic Carbon Dioxide Reduction. *Chem. Sci.* **2020**, *11* (2), 543−550.
(15) Zhang, M.; Lu, M.; Lang, Z.-L.; Liu, J.; Liu, M.; Chang, J.-N.; Li, L.-Y.; Shang, L.-J.; Wang, M.; Li, S.-L.; Lan, Y.-Q. Semiconductor/Covalent-Organic-Framework Z-Scheme Heterojunctions for Artificial Photosynthesis. *Angew. Chem., Int. Ed.* **2020**, *59*, 6500.
(16) Stegbauer, L.; Schwinghammer, K.; Lotsch, B. V. A Hydrazone-Based Covalent Organic Framework for Photocatalytic Hydrogen Production. *Chem. Sci.* **2014**, *5* (7), 2789−2793.
(17) Pachfule, P.; Acharjya, A.; Roeser, J.; Langenhahn, T.; Schwarze, M.; Schomäcker, R.; Thomas, A.; Schmidt, J. Diacetylene Functionalized Covalent Organic Framework (COF) for Photocatalytic Hydrogen Generation. *J. Am. Chem. Soc.* **2018**, *140* (4), 1423−1427.
(18) Bhunia, S.; Das, S. K.; Jana, R.; Peter, S. C.; Bhattacharya, S.; Addicoat, M.; Bhaumik, A.; Pradhan, A. Electrochemical Stimuli-Driven Facile Metal-Free Hydrogen Evolution from Pyrene-Porphyrin-Based Crystalline Covalent Organic Framework. *ACS Appl. Mater. Interfaces* **2017**, *9* (28), 23843−23851.
(19) Wang, D.; Streater, D.; Peng, Y.; Huang, J. 2D Covalent Organic Frameworks with an Incorporated Manganese Complex for Light Driven Carbon Dioxide Reduction. *ChemPhotoChem.* **2021**, *5* (12), 1119−1123.
(20) Tran, L. D.; Presley, K. F.; Streit, J. K.; Carpena-Núñez, J.; Beagle, L. K.; Grusenmeyer, T. A.; Dalton, M. J.; Vaia, R. A.; Drummy, L. F.; Glavin, N. R.; Baldwin, L. A. Divergent Properties in Structural Isomers of Triphenylamine-Based Covalent Organic Frameworks. *Chem. Mater.* **2022**, *34* (2), 529−536.
(21) Yang, J.; Ghosh, S.; Roeser, J.; Acharjya, A.; Penschke, C.; Tsutsui, Y.; Rabeah, J.; Wang, T.; Djoko Tameu, S. Y.; Ye, M. Y.; Grüneberg, J.; Li, S.; Li, C.; Schomäcker, R.; Van De Krol, R.; Seki, S.; Saalfrank, P.; Thomas, A. Constitutional Isomerism of the Linkages in Donor−Acceptor Covalent Organic Frameworks and Its Impact on Photocatalysis. *Nat. Commun.* **2022**, *13* (1), 1.
(22) Vardhan, H.; Al-Enizi, A. M.; Nafady, A.; Pan, Y.; Yang, Z.; Gutiérrez, H. R.; Han, X.; Ma, S. Single-Pore versus Dual-Pore Bipyridine-Based Covalent−Organic Frameworks: An Insight into the Heterogeneous Catalytic Activity for Selective C—H Functionalization. *Small* **2021**, *17* (22), No. 2003970.
(23) Wang, X.; Fu, Z.; Zheng, L.; Zhao, C.; Wang, X.; Chong, S. Y.; McBride, F.; Raval, R.; Bilton, M.; Liu, L.; Wu, X.; Chen, L.; Sprick, R. S.; Cooper, A. I. Covalent Organic Framework Nanosheets Embedding Single Cobalt Sites for Photocatalytic Reduction of Carbon Dioxide. *Chem. Mater.* **2020**, *32* (21), 9107−9114.
(24) Ruan, X.; Yang, Y.; Liu, W.; Ma, X.; Zhang, C.; Meng, Q.; Wang, Z.; Cui, F.; Feng, J.; Cai, F.; Yuan, Y.; Zhu, G. Mechanical Bond Approach to Introducing Self-Adaptive Active Sites in Covalent Organic Frameworks for Zinc-Catalyzed Organophosphorus Degradation. *ACS Cent Sci.* **2021**, *7* (10), 1698−1706.
(25) Leng, W.; Peng, Y.; Zhang, J.; Lu, H.; Feng, X.; Ge, R.; Dong, B.; Wang, B.; Hu, X.; Gao, Y. Sophisticated Design of Covalent Organic Frameworks with Controllable Bimetallic Docking for a Cascade Reaction. *Chem.− Eur. J.* **2016**, *22* (27), 9087−9091.
(26) Zhang, M.; Chen, J.; Zhang, S.; Zhou, X.; He, L.; Sheridan, M. V.; Yuan, M.; Zhang, M.; Chen, L.; Dai, X.; Ma, F.; Wang, J.; Hu, J.; Wu, G.; Kong, X.; Zhou, R.; Albrecht-Schmitt, T. E.; Chai, Z.; Wang, S. Electron Beam Irradiation as a General Approach for the Rapid Synthesis of Covalent Organic Frameworks under Ambient Conditions. *J. Am. Chem. Soc.* **2020**, *142* (20), 9169−9174.
(27) Popov, D. A.; Luna, J. M.; Orchanian, N. M.; Haiges, R.; Downes, C. A.; Marinescu, S. C. A 2,2′-Bipyridine-Containing Covalent Organic Framework Bearing Rhenium(i) Tricarbonyl Moieties for CO2 Reduction. *Dalton Transactions* **2018**, *47* (48), 17450−17460.
(28) Shinde, D. B.; Aiyappa, H. B.; Bhadra, M.; Biswal, B. P.; Wadge, P.; Kandambeth, S.; Garai, B.; Kundu, T.; Kurungot, S.; Banerjee, R. A Mechanochemically Synthesized Covalent Organic Framework as a Proton-Conducting Solid Electrolyte. *J. Mater. Chem. A Mater.* **2016**, *4* (7), 2682−2690.
(29) Bhadra, M.; Sasmal, H. S.; Basu, A.; Midya, S. P.; Kandambeth, S.; Pachfule, P.; Balaraman, E.; Banerjee, R. Predesigned Metal-Anchored Building Block for In Situ Generation of Pd Nanoparticles in Porous Covalent Organic Framework: Application in Heterogeneous Tandem Catalysis. *ACS Appl. Mater. Interfaces* **2017**, *9* (15), 13785−13792.
(30) Jati, A.; Dey, K.; Nurhuda, M.; Addicoat, M. A.; Banerjee, R.; Maji, B. Dual Metalation in a Two-Dimensional Covalent Organic Framework for Photocatalytic C−N Cross-Coupling Reactions. *J. Am. Chem. Soc.* **2022**, *144* (17), 7822−7833.
(31) Han, Y.; Di, J.-Q.; Zhao, A.-D.; Zhang, Z.-H. Synthesis, Characterization and Catalytic Performance of Palladium Supported on Pyridine-Based Covalent Organic Polymer for Suzuki-Miyaura Reaction. *Appl. Organomet. Chem.* **2019**, *33* (10), No. e5172.
(32) Wang, R.; Kong, W.; Zhou, T.; Wang, C.; Guo, J. Organobase Modulated Synthesis of High-Quality β-Ketoenamine-Linked Covalent Organic Frameworks. *Chem. Commun.* **2021**, *57* (3), 331−334.
(33) Chen, H.; Gu, Z.-G.; Zhang, J. Chiral-Induced Ultrathin Covalent Organic Frameworks Nanosheets with Tunable Circularly Polarized Luminescence. *J. Am. Chem. Soc.* **2022**, *144* (16), 7245−7252.
(34) Lu, Z.; Yang, H.; Fu, X.; Zhao, Y.; Xiao, L.; Zhang, Z.; Hou, L. Visible Light-Regulated Heterogeneous Catalytic PET-RAFT by High

https://doi.org/10.1021/jacs.3c10627
J. Am. Chem. Soc. XXXX, XXX, XXX−XXX

Crystallinity Covalent Organic Framework. *Macromol. Rapid Commun.* **2021**, *42* (20), No. 2100384.
(35) Wang, N.; Liu, J.; Tang, L.; Wei, X.; Wang, C.; Li, X.; Ma, L. Facile Synthesis of Rh Anchored Uniform Spherical COF for One-Pot Tandem Reductive Amination of Aldehydes to Secondary Imines. *ACS Appl. Mater. Interfaces* **2021**, *13* (21), 24966−24975.
(36) Kang, C.; Yang, K.; Zhang, Z.; Usadi, A. K.; Calabro, D. C.; Baugh, L. S.; Wang, Y.; Jiang, J.; Zou, X.; Huang, Z.; Zhao, D. Growing Single Crystals of Two-Dimensional Covalent Organic Frameworks Enabled by Intermediate Tracing Study. *Nat. Commun.* **2022**, *13* (1), 1370.
(37) Nguyen, Q. M.; Abouezzi, J.; Ristroph, L. Early Turbulence and Pulsatile Flows Enhance Diodicity of Tesla's Macrofluidic Valve. *Nat. Commun.* **2021**, *12* (1), 2884.
(38) Natraj, A.; Ji, W.; Xin, J.; Castano, I.; Burke, D. W.; Evans, A. M.; Strauss, M. J.; Ateia, M.; Hamachi, L. S.; Gianneschi, N. C.; ALOthman, Z. A.; Sun, J.; Yusuf, K.; Dichtel, W. R. Single-Crystalline Imine-Linked Two-Dimensional Covalent Organic Frameworks Separate Benzene and Cyclohexane Efficiently. *J. Am. Chem. Soc.* **2022**, *144* (43), 19813−19824.
(39) Asbury, J. B.; Wang, Y.; Lian, T. Time-Dependent Vibration Stokes Shift during Solvation: Experiment and Theory. *Bull. Chem. Soc. Jpn.* **2002**, *75* (5), 973−983.
(40) Johnson, E. M.; Haiges, R.; Marinescu, S. C. Covalent-Organic Frameworks Composed of Rhenium Bipyridine and Metal Porphyrins: Designing Heterobimetallic Frameworks with Two Distinct Metal Sites. *ACS Appl. Mater. Interfaces* **2018**, *10* (44), 37919−37927.
(41) Kurz, P.; Probst, B.; Spingler, B.; Alberto, R. Ligand Variations in [ReX(Diimine)(CO)3] Complexes: Effects on Photocatalytic CO2 Reduction. *Eur. J. Inorg. Chem.* **2006**, *2006* (15), 2966−2974.
(42) Benson, E. E.; Sampson, M. D.; Grice, K. A.; Smieja, J. M.; Froehlich, J. D.; Friebel, D.; Keith, J. A.; Carter, E. A.; Nilsson, A.; Kubiak, C. P. The Electronic States of Rhenium Bipyridyl Electrocatalysts for CO2 Reduction as Revealed by X-Ray Absorption Spectroscopy and Computational Quantum Chemistry. *Angew. Chem., Int. Ed.* **2013**, *52* (18), 4841−4844.
(43) Oppelt, K. T.; Sevéry, L.; Utters, M.; Tilley, S. D.; Hamm, P. Flexible to Rigid: IR Spectroscopic Investigation of a Rhenium-Tricarbonyl-Complex at a Buried Interface. *Phys. Chem. Chem. Phys.* **2021**, *23* (7), 4311−4316.
(44) Cannizzo, A.; Blanco-Rodríguez, A. M.; El Nahhas, A.; Šebera, J.; Záliš, S.; Vlček, A., Jr.; Chergui, M. Femtosecond Fluorescence and Intersystem Crossing in Rhenium(I) Carbonyl−Bipyridine Complexes. *J. Am. Chem. Soc.* **2008**, *130* (28), 8967−8974.
(45) Elstner, M.; Porezag, D.; Jungnickel, G.; Elsner, J.; Haugk, M.; Frauenheim, Th.; Suhai, S.; Seifert, G. Self-Consistent-Charge Density-Functional Tight-Binding Method for Simulations of Complex Materials Properties. *Phys. Rev. B* **1998**, *58* (11), 7260−7268.
(46) Aradi, B.; Hourahine, B.; Frauenheim, Th. DFTB+, a Sparse Matrix-Based Implementation of the DFTB Method. *J. Phys. Chem. A* **2007**, *111* (26), 5678−5684.
(47) Hourahine, B.; Aradi, B.; Blum, V.; Bonafé, F.; Buccheri, A.; Camacho, C.; Cevallos, C.; Deshaye, M. Y.; Dumitrică, T.; Dominguez, A.; Ehlert, S.; Elstner, M.; van der Heide, T.; Hermann, J.; Irle, S.; Kranz, J. J.; Köhler, C.; Kowalczyk, T.; Kubař, T.; Lee, I. S.; Lutsker, V.; Maurer, R. J.; Min, S. K.; Mitchell, I.; Negre, C.; Niehaus, T. A.; Niklasson, A. M. N.; Page, A. J.; Pecchia, A.; Penazzi, G.; Persson, M. P.; Řezáč, J.; Sánchez, C. G.; Sternberg, M.; Stöhr, M.; Stuckenberg, F.; Tkatchenko, A.; Yu, V. W. z.; Frauenheim, T. DFTB+, a Software Package for Efficient Approximate Density Functional Theory Based Atomistic Simulations. *J. Chem. Phys.* **2020**, *152* (12), 124101.
(48) Gaus, M.; Lu, X.; Elstner, M.; Cui, Q. Parameterization of DFTB3/3OB for Sulfur and Phosphorus for Chemical and Biological Applications. *J. Chem. Theory Comput* **2014**, *10* (4), 1518−1537.
(49) Grimme, S.; Antony, J.; Ehrlich, S.; Krieg, H. A Consistent and Accurate Ab Initio Parametrization of Density Functional Dispersion Correction (DFT-D) for the 94 Elements H-Pu. *J. Chem. Phys.* **2010**, *132* (15), 154104.
(50) Grimme, S.; Ehrlich, S.; Goerigk, L. Effect of the Damping Function in Dispersion Corrected Density Functional Theory. *J. Comput. Chem.* **2011**, *32* (7), 1456−1465.
(51) Thomas, S.; Li, H.; Zhong, C.; Matsumoto, M.; Dichtel, W. R.; Bredas, J.-L. Electronic Structure of Two-Dimensional π-Conjugated Covalent Organic Frameworks. *Chem. Mater.* **2019**, *31* (9), 3051−3065.
(52) Feng, T.; Streater, D.; Sun, B.; Duisenova, K.; Wang, D.; Liu, Y.; Huang, J.; Zhang, J. Tuning Photoexcited Charge Transfer in Imine-Linked Two-Dimensional Covalent Organic Frameworks. *J. Phys. Chem. Lett.* **2022**, *13* (6), 1398−1405.
(53) Bauernschmitt, R.; Ahlrichs, R. Treatment of Electronic Excitations within the Adiabatic Approximation of Time Dependent Density Functional Theory. *Chem. Phys. Lett.* **1996**, *256* (4), 454−464.
(54) Casida, M. E.; Jamorski, C.; Casida, K. C.; Salahub, D. R. Molecular Excitation Energies to High-Lying Bound States from Time-Dependent Density-Functional Response Theory: Characterization and Correction of the Time-Dependent Local Density Approximation Ionization Threshold. *J. Chem. Phys.* **1998**, *108* (11), 4439−4449.
(55) Yanai, T.; Tew, D. P.; Handy, N. C. A New Hybrid Exchange−Correlation Functional Using the Coulomb-Attenuating Method (CAM-B3LYP). *Chem. Phys. Lett.* **2004**, *393* (1−3), 51−57.
(56) Ditchfield, R.; Hehre, W. J.; Pople, J. A. Self-Consistent Molecular-Orbital Methods. IX. An Extended Gaussian-Type Basis for Molecular-Orbital Studies of Organic Molecules. *J. Chem. Phys.* **1971**, *54* (2), 724−728.
(57) Krishnan, R.; Binkley, J. S.; Seeger, R.; Pople, J. A. Self-consistent Molecular Orbital Methods. XX. A Basis Set for Correlated Wave Functions. *J. Chem. Phys.* **1980**, *72* (1), 650−654.
(58) Frisch, M. J.; Trucks, G. W.; Schlegel, H. B.; Scuseria, G. E.; Robb, M. A.; Cheeseman, J. R.; Scalmani, G.; Barone, V.; Petersson, G. A.; Nakatsuji, H.; Li, X.; Caricato, M.; Marenich, A. V.; Bloino, J.; Janesko, B. G.; Gomperts, R.; Mennucci, B.; Hratchian, H. P.; Ortiz, J. V.; Fox, D. J., *Gaussian 16 Revision C.01*; Gaussian Inc.: Wallingford, CT, 2016.
(59) Plasser, F. TheoDORE: A Toolbox for a Detailed and Automated Analysis of Electronic Excited State Computations. *J. Chem. Phys.* **2020**, *152* (8), 84108.
(60) Chai, J.-D.; Head-Gordon, M. Long-Range Corrected Hybrid Density Functionals with Damped Atom−Atom Dispersion Corrections. *Phys. Chem. Chem. Phys.* **2008**, *10* (44), 6615−6620.
(61) Clark, T.; Chandrasekhar, J.; Spitznagel, G. W.; Schleyer, P. V. R. Efficient Diffuse Function-Augmented Basis Sets for Anion Calculations. III. The 3-21+G Basis Set for First-Row Elements, Li−F. *J. Comput. Chem.* **1983**, *4* (3), 294−301.
(62) Hay, P. J.; Wadt, W. R. Ab Initio Effective Core Potentials for Molecular Calculations. Potentials for K to Au Including the Outermost Core Orbitals. *J. Chem. Phys.* **1985**, *82* (1), 299−310.
(63) Schuchardt, K. L.; Didier, B. T.; Elsethagen, T.; Sun, L.; Gurumoorthi, V.; Chase, J.; Li, J.; Windus, T. L. Basis Set Exchange: A Community Database for Computational Sciences. *J. Chem. Inf Model* **2007**, *47* (3), 1045−1052.
(64) Feller, D. The Role of Databases in Support of Computational Chemistry Calculations. *J. Comput. Chem.* **1996**, *17* (13), 1571−1586.
(65) Pritchard, B. P.; Altarawy, D.; Didier, B.; Gibson, T. D.; Windus, T. L. New Basis Set Exchange: An Open, Up-to-Date Resource for the Molecular Sciences Community. *J. Chem. Inf Model* **2019**, *59* (11), 4814−4820.
(66) Martin, R. L. Natural Transition Orbitals. *J. Chem. Phys.* **2003**, *118* (11), 4775−4777.

https://doi.org/10.1021/jacs.3c10627
J. Am. Chem. Soc. XXXX, XXX, XXX−XXX